Dynamic damage analysis of carbon fiber reinforced polymer composite pressure vessels

Kamal M. Hammad*
Center for Digital Engineering, Skoltech, Russia
Kamal.Hammad@skoltech.ru, http://orcid.org0009-0004-6051-5222

Iuliia A. Sadykova
Center for Digital Engineering, Skoltech, Russia; CASM&T, MAI, Russia
iuliia.sadykova@skoltech.ru, https://orcid.org/0009-0003-5796-832X

Eugene N. Prokopev, Galina V. Tyurina
Laboratory of Accelerated Particles <<LUCh>>, NUST MISIS, Russia
syd.ry@mail.ru, alenatyurina15@gmail.com

Semen D. Ignatyev
FBES FSCH named after F.F. Erisman of the Rospotrebnadzor, Mytishchi, Russia
ignatyev.s.11@gmail.com, https://orcid.org/0000-0001-7415-5513

Eugene S. Statnik
Center for Digital Engineering, Skoltech, Russia; CASM&T, MAI, Russia; Laboratory of Accelerated Particles <<LUCh>>, NUST MISIS, Russia
Eugene.Statnik@skoltech.ru, https://orcid.org/0000-0002-1105-9206

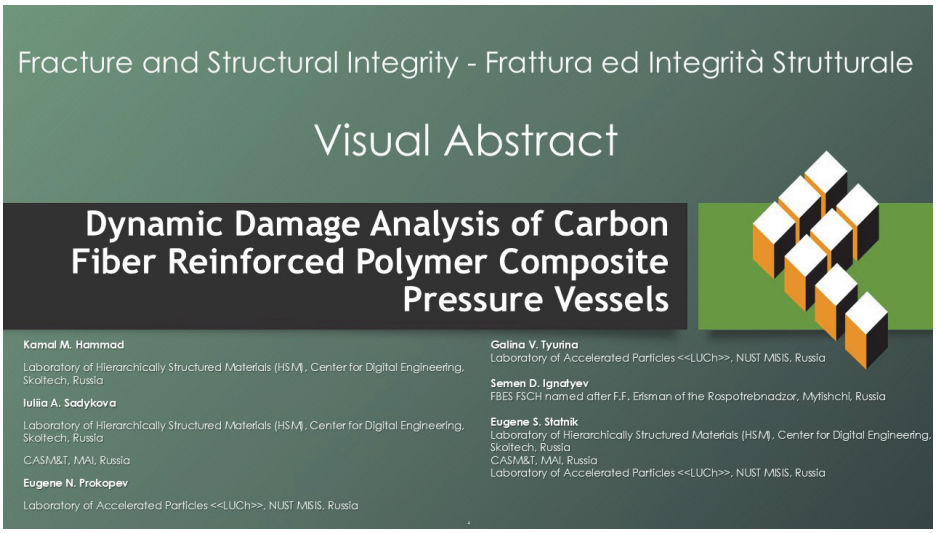

Citation: Hammad, K. M., Sadykova, I. A., Prokopev, E. N., Tyurina, G. V., Ignatyev, . D., Statnik, E., Dynamic damage analysis of carbon fiber reinforced polymer composite pressure vessels , Fracture and Structural Integrity, 74 (2025) 321-341.

Received: 27.06.2025
Accepted: 06.09.2025
Published: 09.09.2025
Issue: 10.2025

KEYWORDS. CFRP, Composite pressure vessels, Spall damage, Explosive loading, Dynamic impact, Numerical simulation, Coupled Eulerian–Lagrangian (CEL), Abaqus/Explicit, Intralaminar damage, Hashin criterion, interlaminar damage, Virtual Crack Closure Technique (VCCT)

INTRODUCTION

Carbon Fiber Reinforced Polymers (CFRPs) are widely utilized in various industries due to their exceptional strength-to-weight and stiffness-to-weight ratios, making them ideal for a range of demanding applications [1]. One of the critical uses of CFRPs is the construction of confinement vessels, which play a vital role in preventing catastrophic events and containing explosion debris [2]. Consequently, understanding the behavior of CFRP pressure vessels under dynamic loading conditions is essential for ensuring their safety and reliability. However, experimental testing of such parts under representative deformation rates is often expensive and resource-intensive, leading to a growing trend toward reducing destructive testing through the development of high-fidelity Finite Element Analysis (FEA) models [3]. These models offer numerous advantages, including cost-effectiveness by minimizing material waste and energy consumption, improved safety, and accelerated research and development processes. The principal requirement for the use of such models for design is the confirmation of their validity through rational experimental-computational correlation (RECC) [4].

The behavior of CFRP pressure vessels is characterized by significant complexity, influenced by such factors as the number of layers, fiber orientation, and loading rate [5–7]. Experimental investigations, including the use of the split-Hopkinson pressure bar technique, have demonstrated that strain rate plays a critical role in determining the post-impact residual strength and fracture resistance of these materials [8]. Specifically, increased strain rates could enhance the elastic modulus and tensile strength of CFRP composite materials, due to the influence of strain rate on the deformation and damage characteristics of composites [9], [10]. Such high-strain-rate loading conditions are commonly observed in impact scenarios, particularly within the automotive and aerospace industries, where pressure vessels are often subjected to extreme dynamic loads. To accurately predict the material behavior under these conditions, constitutive material models have been developed [7], [11]. Among these, the Johnson-Cook [12] and Zerilli-Armstrong [13] models have been extensively employed to analyze the dynamic response of CFRP composite tubes under axial impact loading.

Impact-induced damage in composite materials can be categorized into in-plane (intralaminar) damage and interlaminar damage, the latter often referred to as spallation. Spallation occurs when material layers delaminate due to high-impact loading. While previous studies have attempted to model impact damage in composite materials [14], inconsistencies remain in accurately representing intralaminar damage, fiber failure, and matrix cracking. Recent applications of advanced composite-reinforced structures in structural analysis, such as in [15-18] highlight the importance of accurate simulation methods with integrated micromechanical based modeling for predicting damage, free vibration and thermomechanical behavior under severe dynamic loads. Additionally, Fedorenko *et al.* [19] investigated the behavior of filament-wound T700/LY113 carbon/epoxy composites under shock loading using the electric wire explosion method used in [20], revealing the significant influence of strain rate on the post-impact strength. This study [19] presented valuable experimental data, but did not provide a comprehensive analysis of the intralaminar or interlaminar damage mechanisms.

The present study bridges this gap and builds upon previous research by investigating the effects of high strain rates induced by internal blast loading on CFRP pressure vessels, with a particular focus on the circumferential strain evolution and the concurrent development of intralaminar and interlaminar damage exploiting both Hashin and VCCT criteria, respectively. For modeling CFRP structures under blast and dynamic loading, it is commonly accepted to combine the use of the Virtual Crack Closure Technique (VCCT) for interlaminar delamination and the Hashin criteria for intralaminar damage. Nevertheless, each method has certain presumptions and restrictions. Although it is not necessarily rate-dependent and may need to be extended for high strain-rate applications, Hashin damage model is effective for predicting intralaminar damage because it is physically based and differentiates between fiber and matrix failure modes. While the Tsai–Wu criterion provides a more general but less physically descriptive interaction-based failure prediction, other criteria, like the Puck model, are frequently better suited for matrix-dominated failures or situations involving strong fiber-matrix interfaces. Cohesive zone models (CZM) provide more flexibility for complex crack paths by simulating both crack initiation and growth, whereas VCCT is reliable in capturing crack propagation for delamination modeling. However, fracture toughness, which is known to be strain-rate sensitive, must be accurately characterized for both VCCT and CZM. Static formulations are unable to adequately capture additional inertial effects that may impact delamination growth under blast and high-velocity impact loading. Consequently, the primary failure mechanisms must be taken into account when choosing a model:

Puck may perform better in matrix-dominated situations, Hashin is usually effective for fiber/matrix failures, and CZM offers benefits over VCCT when nonlinear crack evolution is substantial [21]. Although its application at high strain rates requires careful calibration and awareness of inherent limitations, the combined Hashin–VCCT framework is chosen because it has been extensively validated for CFRPs under dynamic conditions.

The work of Fedorenko et al. [19] is utilized as the source of information regarding the material properties, experimental configuration, modeling approach, and key relationships. Major additional developments are introduced to enhance the accuracy of numerical simulations. The main purpose of the present paper is to validate complex models based on the RECC approach. The novelty of this work lies in the successful concurrent utilization of the two damage criteria: Hashin's failure criterion for intralaminar damage, and the Virtual Crack Closure Technique (VCCT) for modeling interlaminar delamination in a CEL framework. The results demonstrate improved agreement with experimental data compared to previous studies, particularly in modeling damage patterns observed in explosion shock pulse experiments. This research contributes to the ongoing effort to formulate and validate accurate predictive models for CFRP structures subjected to extreme dynamic loads.

MATERIALS AND METHODS

Pressure vessel model

The numerical model used in this study was developed based on the experimental configuration described in [19]. All modeling and simulations were conducted using Abaqus/Explicit FEA software (version 2021) on a high-performance computer [22]. The pressure vessel (p.v.) exploding-wire sudden internal pressurization model setup consists of a carbon fiber reinforced polymer (CFRP) composite p.v. shell, a PMMA solid tube insert, and a Eulerian domain representing the vapor generated from the explosion of the copper wire. The sketch of the model with characteristic dimensions as well as the numerical assembly is illustrated in Fig. 1. The copper wire positioned inside the tube insert is represented by the Eulerian domain that represents the vapor resulting from the wire explosion. In Eulerian analysis, nodes remain fixed, and material flows through non-deforming elements, whereas in Lagrangian analysis, nodes move with the material. In the real experiment, the copper wire is subjected to a sudden discharge voltage to stimulate an internal explosion. Together with the PMMA cylindrical insert this assembly ensures the passage of the pressure pulse to the CFRP shell, and replicates the important real-life scenario of pressure vessel suffering abrupt internal pressurization due to the explosion of contained reactive chemicals or due to the externally triggered incendiary event. CFRP structures investigated in this study featured two different winding arrangements, namely, with uniaxial fiber reinforcement in the circumferential orientation ($[0^{\circ}]_{10}$) and an angle-ply orientation with two directions, $[+45^{\circ}/-45^{\circ}]_5$. Both samples of $[0^{\circ}]_{10}$ and $[+45^{\circ}/-45^{\circ}]_5$ orientations had the overall thickness of 1 mm. The thickness of each ply was 0.1 mm.

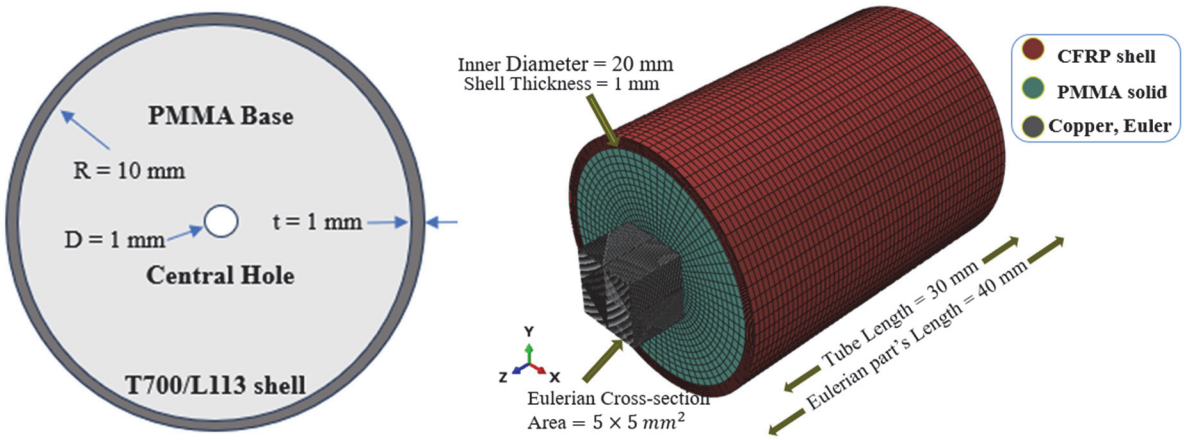

(a) (b)

Figure 1: The geometry of (a) the specimen under experimental investigation, and (b) the FE numerical model assembly.

Since a single homogeneous set cannot accurately represent the structure of the composite shell due to the variation in mechanical properties between individual layers, and because we are concerned about failure that happens by delamination due to weakened interfaces between plies; each layer must be modeled with its own set of elements [23]. In this study, the composite shell layup was modeled using 10 separate rings, each with its respective orientation prescribed, as illustrated in

Fig. 2. The initial mesh (coarse) for each composite ring consists of 4000 reduced continuum shell elements in the Lagrangian formulation (designated as SC8R in Abaqus, Simulia Inc.), with the sectional circumference discretized into 80 elements and the element dimension along the z-axis (longitudinal axis of the cylinder) is 0.6 mm. By giving each ply a local material coordinate system, the finite element model explicitly took into account the various fiber orientations, guaranteeing that the orthotropic properties matched the actual fiber directions. Two layup configurations were examined after modeling the composite shell as a stack of ten different plies: a unidirectional $[0^\circ]_{10}$ stack, where all plies were oriented along the vessel hoop (circumferential) direction; and an angle-ply $[+45^\circ/-45^\circ]_5$ stack, where the plies alternated between $+45^\circ$ and -45° with respect to the hoop direction.

The "orientation" keyword in Abaqus/Explicit was used to assign a local material orientation to each ply. The ply fiber direction and the fiber axis (1-direction) were lined up, and the rotation plane was established by defining a reference axis in the global cylindrical coordinate system, usually the vessel axial direction. The fiber axis was then rotated to its correct orientation using the designated rotation angle (0°, $+45^\circ$, or -45°). This process made sure that the Hashin damage criteria, which rely on stresses in the local coordinate system, and the stiffness matrix (with maximum stiffness E_1 along the fiber axis) were accurately assessed for every ply. This method is shown in Fig. 3, where the local directions are indicated by arrows: red for the radial direction (3-axis), yellow for the in-plane transverse direction (2-axis), and blue for the fiber direction (1-axis). The model represents the anisotropic response of each ply by explicitly assigning material orientations, avoiding homogenization assumptions. Because of the accuracy in defining fiber orientation, this method is crucial for precisely forecasting both intralaminar failure and interlaminar delamination.

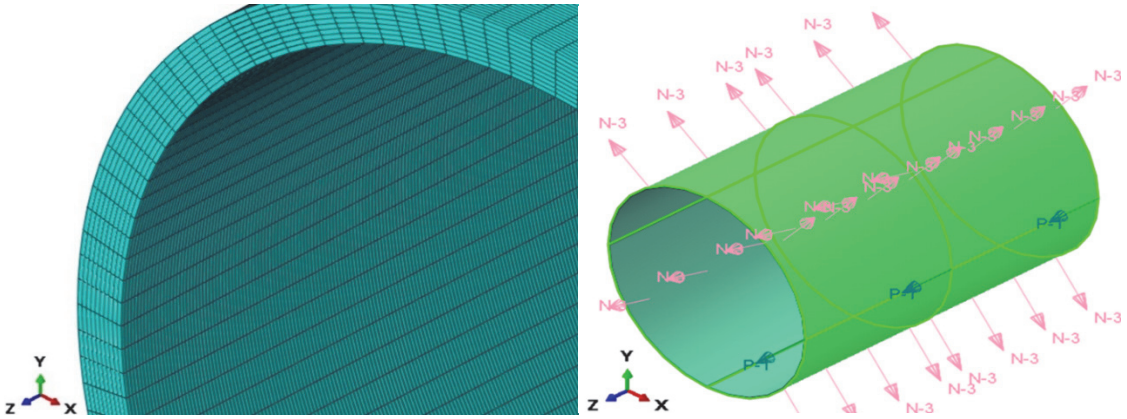

(a) (b)

Figure 2: (a) The illustration of the mesh used for the composite vessel CFRP shell, consisting of 10 cylindrical layers, with (b) their discrete field.

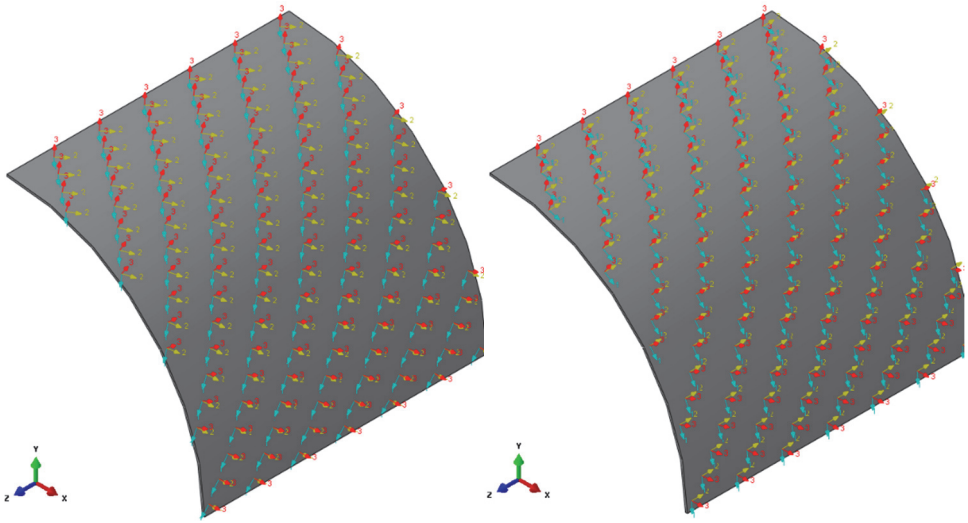

(a) (b)

Figure 3: The material orientations (winding direction) of : (a) the $\pm 45^\circ$ (angle-ply) plies and (b) the 0° (hoop-direction) plies.

The initial mesh (coarse) of the PMMA section was composed of 80000 reduced solid elements (designated as C3D8R in the notation of Abaqus, Simulia Inc.) as shown in Fig. 4(a). In "Region 1", comprising the surrounding of the central hole, the mesh size evolves, from in out, from 0.2 mm to 0.3 mm, while in "Region 2", it evolves from 0.45 mm to 0.7 mm along the same direction. The PMMA insert experiences large deformations, wave propagation, and material failure (modeled with JH-2). The C3D8R element is robust and efficient for such large-strain, explicit dynamics simulations involving complex constitutive models and element deletion. The inner channel section representing the fixed space which will be occupied by the copper vapor during its expansion is referred to as the Eulerian part. Beyond its volume, the vapor pressure is deemed insignificant for further examination. As shown in Fig. 4(b), the Eulerian part is modeled using 1440000 cuboid elements, each with a side length of 0.1 mm, in the Eulerian formulation (denoted as EC3D8R in Abaqus notation). The EC3D8R element is the standard first-order brick element for Eulerian analyses in Abaqus. Moreover, the Eulerian formulation is necessary to handle the extreme deformation and flow of the vaporized wire products without the mesh distortion problems that would cripple a Lagrangian mesh.

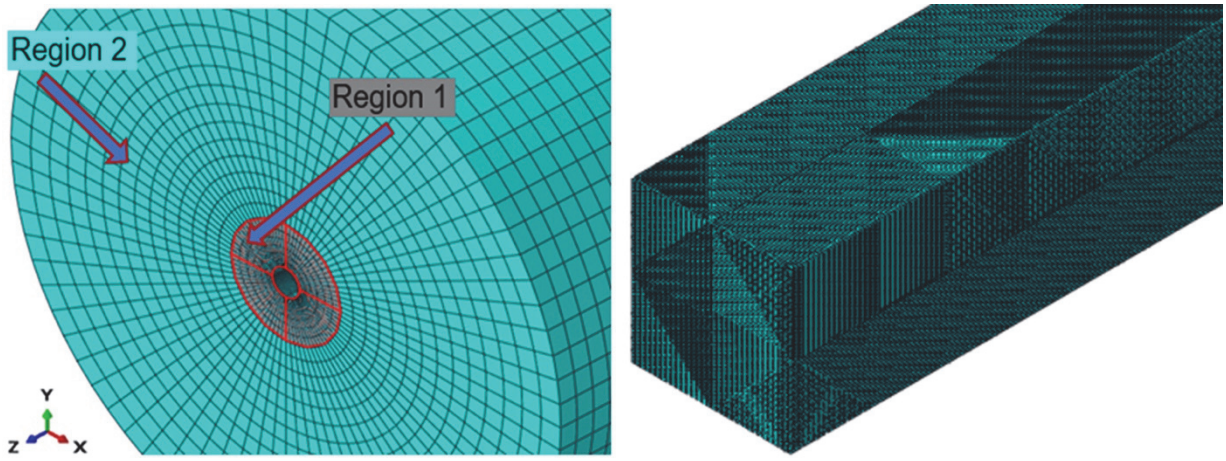

(a) (b)

Figure 4: The mesh configurations (a) for the PMMA insert, and (b) Eulerian part.

The reason of representing the p.v. with continuum shell elements (SC8R) is that they provide a computationally effective way to simulate three-dimensional systems on a local level, such as a multilayered laminated composite structure. They combine the three-dimensional geometry of solid elements with the planar nature of conventional shells, making them suitable for global analyses rather than local failure predictions. These elements allow mechanical and/or thermal loading for both static and dynamic procedures, with only displacement degrees of freedom. They also use linear interpolation and are suitable for nonlinear geometric analysis due to their ability to accommodate large rotations, finite membrane deformation, and the consequences of thickness change and transverse shear deformation. Continuum shell elements utilize first-order layer-wise composite theory, allowing for a refined radial response and more accurate transverse shear stress and force prediction by stacking them, unlike conventional shells [22].

A mesh study analysis is essential in FEA simulations, so failure stresses are compared based on changing the mesh size. So, medium and fine mesh configurations are created for the 2 structures, the $[+45°/-45°]_5$, and the $[0°]_{10}$ orientated structures. The fine mesh of each composite ring consists of 49600 continuum shell elements; the circumference consists of 124 elements; and the along-z-axis element dimension is 0.075 mm. The along-z-axis element dimension and number of elements along the circumference for both the PMMA and composite rings are kept equal to ensure better bond separation during spall analysis. Regarding the PMMA insert, , the element length of the refined PMMA mesh was set to 0.08 mm in the radial direction in zone 1 to ensure accurate representation. Zone 2 grew in element size beyond this zone, from 0.22 mm to 0.4 mm, for elements at the outer surface of the cylinder. Furthermore, a stacking direction is introduced to the model to be from bottom to top, which is logical regarding the internal blast loading inside the vessel. The Eulerian mesh is kept the same because it was made as fine as possible from the beginning of the simulation to ensure having accurate results.

The intermediate mesh of each composite ring consists of 20000 continuum shell elements; the circumference consists of 100 elements; and the along-z-axis element dimension is 0.150 mm. In zone 1, the element length of the refined PMMA mesh was set to 0.150 mm in the radial direction to ensure accurate representation. Zone 2 grew in element size beyond this zone, from 0.23 mm to 0.44 mm, for elements at the outer surface of the cylinder. The main mesh parameters of both the p.v. and the PMMA insert are summarized in Tab. 1.

Component	Mesh Level	Elements	Longitudinal Element Size (mm)	Circumferential Elements	Radial Element Size (mm)
Composite Rings	Coarse	4000	0.60	80	0.1
	Medium	20000	0.15	100	0.1
	Fine	49600	0.075	124	0.1
PMMA Insert	Coarse	180000	0.6	80	0.2-0.3 (Zone 1); 0.45-0.7 (Zone 2)
	Medium		0.15	100	0.15 (Zone 1); 0.23-0.44 (Zone 2
	Fine		0.075	124	0.08 (Zone 1); 0.22-0.4 (Zone 2)

Table 1: Summarized mesh study parameters.

Material Properties

The PMMA material properties, the CFRP elastic properties and strength under quasi-static loading conditions for the simulation were taken from [19] and are summarized in Tabs. 2, 3 and 4, respectively. The elastic engineering constants in Tab. 3 represent the longitudinal elasticity modulus (E_1), the transverse elasticity moduli (E_2 and E_3), Poisson's ratios (ν) and shear moduli (G) in all the respective local directions. The in-plane shear modulus G_{12} (3200 MPa) was given the same value as the transverse shear moduli G_{13} and G_{23}. When precise radial shear test data is not available, macro-scale composite modeling frequently uses this simplification, which makes the assumption that the material is transversely isotropic with regard to shear behavior [24]. It is justified for this study because the model is less sensitive to the exact value of G_{23} because the main failure modes of interest: intralaminar damage and delamination are primarily driven by in-plane stresses and VCCT Mode-I fracture.

Parameter	Value
Density, ϱ [kg/m^3]	1185
Longitudinal wave speed, c_l [m/s]	2750
Shear wave speed, c_s [m/s]	1400
Bulk modulus, K_1 [GPa]	5.86
Polynomial EOS constant, K_2 [GPa]	24.68
Polynomial EOS constant, K_3 [GPa]	14.5
Shear modulus, G [GPa]	2.32
Hugoniot elastic limit (HEL), [MPa]	750
Deviatoric stress at HEL, [MPa]	520
Intact strength constant, A	1.01
Intact strength exponent, N	0.7
Strain rate constant, C	0.005
Fractured strength constant, B	0.34
Fractured strength exponent, M	0.57
Max. fractured strength ratio, $\sigma^*_{f\,max}$	1
Hydrostatic tensile limit, [MPa]	55
Bulking constant, β	1
Damage constant, D_1	0.005
Damage constant, D_2	0.7
Equivalent plastic strain to fracture under constant pressure (FEA element deletion threshold), ε_p^{max}	0.5
Maximum bound of equivalent plastic strain to fracture under constant pressure, $\varepsilon^f_{p,max}$	0.5

Table 2: PMMA parameters used for the model [19].

E_1, MPa	E_2, MPa	E_3, MPa	ν_{12}	ν_{13}	ν_{23}	G_{12}, MPa	G_{13}, MPa	G_{23}, MPa
126000	8250	8250	0.33	0.30	0.30	3200	3200	3200

Table 3: Elastic engineering constants of the used CFRP material [19].

Longitudinal tensile strength (X^t), MPa	Longitudinal compressive strength (X^c), MPa	Transverse tensile strength (Y^t), MPa	Transverse compressive strength (Y^c), MPa	Longitudinal shear strength (S^L), MPa	Transverse shear strength (S^T), MPa
1898	622	18	125	48	48

Table 4: Longitudinal and transverse strength of the used CFRP material [19].

For CFRP, the intralaminar fracture energies that represent Hashin were initially calibrated based on [25]. This calibration was followed by extensive trial and error simulations to match the experimental data and damage profiles in [19], and the used values in the FE simulations are given in Tab. 5.

Longitudinal Tensile Fracture Energy, N/mm	Longitudinal Compressive Fracture Energy, N/mm	Transverse Tensile Fracture Energy, N/mm	Transverse Compressive Fracture Energy, N/mm
100	5	0.969	11.5

Table 5: Damage-evolution fracture energies of the composite material used in Hashin model [25].

The response of the PMMA insert was modeled using the Johnson–Holmquist (JH-2) constitutive formulation [19], which accounts for high strain-rate effects, damage evolution, and brittle fracture. This implementation captures the volumetric, deviatoric, and damage-dependent behavior of PMMA subjected to shock and impact loading. The volumetric response was represented using a polynomial EOS, consistent with the JH-2 model where the pressure (P) is defined as:

$$P = K_1\mu + K_2\mu^2 + K_3\mu^3, \mu = \frac{\rho}{\rho_0} - 1 \tag{1}$$

for intact material (damage parameter (D)=0), and:

$$P = K_1\mu + K_2\mu^2 + K_3\mu^3 + \Delta P \tag{2}$$

for damaged states ($0 \leq D \leq 1$), where K_1 represents the bulk modulus while K_2 and K_3 are EOS constants that are derived from PMMA Hugoniot data [19]. μ is the volumetric strain; ϱ_0 and ϱ are the reference and current density values; and ΔP is an additional pressure term accounting for bulking and dilatation effects during fracture:

$$\Delta P_{(t+\Delta t)} = -K_1\mu_{t+\Delta t} + \sqrt{(K_1(\mu_{(t+\Delta t)} + \Delta P_t)^2 + 2\beta K_1 \Delta U)} \tag{3}$$

where β is the elastic energy loss parameter and ΔU is the energy increment.
Regarding strength and damage, the normalized stresses σ_i^*, σ^*, and σ_f^* out of the von Mises equivalent stresses σ_i, σ, and σ_f express the strength of intact, damaged, and fractured PMMA, respectively, as:

$$\sigma_i^* = A(1 + C\ln\dot{\varepsilon}^*)(T^* + P^*)^N$$

$$\sigma^* = \sigma_i^* + D(\sigma_f^* - \sigma_i^*) \tag{4}$$

$$\sigma_f^* = B(P^*)^M(1 + C\ln\dot{\varepsilon}^*)$$

where A, B, C, M, N are material constants, T^* is the maximum tensile hydrostatic pressure that the material can endure, p^* is the normalized pressure, and ε^* is the normalized of equivalent strain rate through dividing the strain rate by a reference value equal to 1 s^{-1}. Normalization is performed with respect to the Hugoniot elastic limit (HEL):

$$\sigma_i^* = \frac{\sigma_i}{\sigma_{HEL}}, \sigma^* = \frac{\sigma}{\sigma_{HEL}}, \sigma_f^* = \frac{\sigma_f}{\sigma_{HEL}}, P^* = \frac{P}{P_{HEL}}, T^* = \frac{T}{P_{HEL}}$$

$$\sigma_{HEL} = P_{HEL} + \frac{2}{3} s_{HEL} \tag{5}$$

where σ_{HEL}, p_{HEL}, and s_{HEL}, respectively, are the equivalent stress, volumetric pressure and deviatoric stress at HEL while P is the actual pressure and T is the tensile strength.
Damage accumulation was calculated incrementally as:

$$D = \sum \frac{\Delta \varepsilon_p}{\varepsilon_p^f} \tag{6}$$

where $\Delta\varepsilon_p$ is the plastic strain increment, and ε_p^f is the strain to fracture expressed as:

$$\varepsilon_p^f = D_1 (T^* + P^*)^{D_2} \tag{7}$$

where D_1 and D_2 are PMMA fracture constants and when D is equal to 1, the material is already fractured.

Damage criteria

The experimental testing evidence in [19] shows that both types of damage; interlaminar and intralaminar, occur at a high strain rate during blast loading, so a faithful model should contain them in numerical representation. Using continuum shell elements, the delamination damage was modelled using the Virtual Crack Closure Technique (VCCT), while the intralaminar damage was modeled according to the Hashin failure criterion. To avoid mesh distortion problems, a Coupled Eulerian-Lagrangian (CEL) analysis was applied, in which the Copper vapor at the Eulerian part region was simulated using Eulerian mesh while the PMMA was represented according to the Lagrangian formulation. The application of the CEL analysis allows for efficient contact conditions between the Eulerian and Lagrangian parts, allowing for the efficient transfer of pressure between the PMMA/vapor phases, especially after the fully fractured PMMA elements are excluded from the analysis.
For VCCT-based interlaminar damage, a general self-contact interaction with default interaction properties was defined at the initial step for the tube mesh which consists of the PMMA tube and the composite thin cylinder. In Step 1, this general contact was modified to include the 9 contact surface pairs of the 10 composite layers, ensuring that each ring surface interacted with the opposite surface of the adjacent ring. An interaction property incorporating both cohesive behavior and VCCT debonding criteria was defined for these nine new contact pairs. Potential crack surfaces are bonded in Abaqus/Explicit using the general contact's definition. The capability is applied through a pure main-secondary formulation. To explicitly identify the crack tips, the predefined crack surfaces are assumed to be initially partially bonded. Defining the initially bonded node set, a contact clearance is first defined, then assigned to each of the 9 general contact pairs that each of them consists of two single-sided surfaces. This is how the initial crack is defined. The section that is not bonded functions like a typical contact surface. It is assumed that the nodes in the node set are initially bonded in every direction.
The specified node set is part of the secondary surface, which has to extend beyond it. If not, the crack cannot spread, and the surfaces cannot not debond. The bonded set is shown in Fig. 5, illustrating the initial created crack. This initial clearance value is assigned to each of the 9 contact pairs. The definition of the crack propagation capability was finished by defining a cohesive behavior, based on fracture, to the surface interaction. It was assigned to each pair of initially partially bonded surfaces to initiate the crack propagation. Between these two surfaces, crack propagation takes place when the fracture criterion is satisfied. The of the bonds' elastic behavior is also described by cohesive behavior.

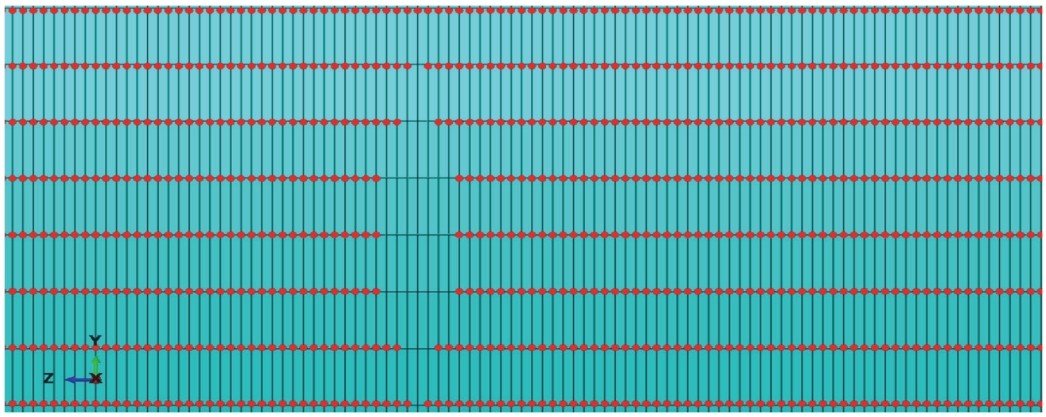

Figure 5: The initial bonded node set defining the initial crack between concentric rings (side-view).

When the fracture criterion parameter (*f*) of VCCT approaches 1.0 within a specified tolerance, the crack-tip node starts debonding as according to:

$$f_{LL} \le f \le f_{UL} \tag{8}$$

where $f_{LL} = 1$ is f upper limit and $f_{UL} = 1 + f_{tol}$ is the upper limit, where f_{tol} is the tolerance parameter whose default value is taken as 0.20, the default in Abaqus. In the general case when three modes of fracture are considered, f is defined as:

$$f = \frac{g_{equiv}}{g_{C,equiv}} \ge 1 \tag{9}$$

where the nodal equivalent strain energy-release rate is g_{equiv}, and the critical equivalent strain energy release rate is $g_{C,equiv}$ which is determined by the interface bond strength and the user-specified mode-mix criterion. In this study $g_{C,equiv}$ is evaluated by the formula of Benzeggagh and Kenane (BK) [26], as in Eqns. (10) and (11), where g_I, g_{II} and g_{III} are the energy-release rate values of the three modes of fracture, while g_{IC}, g_{IIC}, and g_{IIIC} are their critical values, correspondingly. $g_{IC} = 950$ J/m^2 and $g_{IIC} = g_{IIIC} = 1250$ J/m^2 are the chosen critical energy-release rates according to [27] because of the similarity in used materials.

$$g_{C,equiv} = g_{IC} + (g_{IIC} - g_{IC})\left(\frac{g_{II} + g_{III}}{g_I + g_{II} + g_{III}}\right) \tag{10}$$

$$g_{equiv} = g_I + g_{II} + g_{III} \tag{11}$$

In intralaminar damage analysis based on Hashin's damage criteria, the fibers in fiber-reinforced materials are usually thought to be parallel, and degradation at a point is referred to as damage initiation. Material stiffness deterioration is a crucial sign of damage in the analysis of composite materials reinforced with fibers. Elastic-brittle behavior is dominant in unidirectional fiber-reinforced composite materials. Damage to such materials occurs without significant plastic deformation. As a result, when simulating the behavior of these materials, plasticity is often overlooked.
The initiation failure criteria of fiber tension, fiber compression, matrix tension and matrix compression, respectively, have the following general forms [22]:

$$\hat{\sigma}_{11} \geq 0 \rightarrow F_f^t = (\frac{\hat{\sigma}_{11}}{X^t})^2 + \alpha(\frac{\hat{\tau}_{12}}{S^L})^2$$

$$\hat{\sigma}_{11} < 0 \rightarrow F_f^c = (\frac{\hat{\sigma}_{11}}{X^c})^2$$

$$\hat{\sigma}_{22} \geq 0 \rightarrow F_m^t = (\frac{\hat{\sigma}_{22}}{Y^t})^2 + \alpha(\frac{\hat{\tau}_{12}}{S^L})^2 \quad (12)$$

$$\hat{\sigma}_{22} < 0 \rightarrow F_m^c = (\frac{\hat{\sigma}_{22}}{2S^T})^2 + (\frac{Y^c}{2S^T})^2 - 1 + \frac{\hat{\sigma}_{22}}{Y^c}(\frac{\hat{\tau}_{12}}{S^L})^2$$

where X^t is the longitudinal tensile strength; X^c is the longitudinal compressive strength; Y^t is the transverse tensile strength; Y^c is the transverse compressive strength; S^L is the longitudinal shear strength; S^T is the transverse shear strength; α is the coefficient of shear stress contribution to fiber tensile-initiation criterion; and $\sigma\hat{}_{11}$, $\sigma\hat{}_{22}$, $\tau\hat{}_{12}$ are the effective components of stress tensor ($\sigma\hat{} = M*\sigma$), where σ is the true stress, and M is the damage operator. M is determined by Eqn. (13):

$$M = \begin{pmatrix} \frac{1}{(1-d_f)} & 0 & 0 \\ 0 & \frac{1}{(1-d_m)} & 0 \\ 0 & 0 & \frac{1}{(1-d_s)} \end{pmatrix}$$

$$\hat{\sigma}_{11} \geq 0 \rightarrow d_f = d_f^t; \hat{\sigma}_{11} < 0 \rightarrow d_f = d_f^c$$

$$\hat{\sigma}_{22} \geq 0 \rightarrow d_m = d_m^t; \hat{\sigma}_{22} < 0 \rightarrow d_m = d_m^c \quad (13)$$

$$d_s = 1 - (1-d_f^t)(1-d_f^c)(1-d_m^t)(1-d_m^c)$$

where d_f, d_m and d_s are the fiber, matrix, and shear damage parameters; while the superscripts t and c refer to tensile and compressive effects, respectively. The values of X^t, X^c, Y^t, Y^c, S^L and S^T used in the current FE study are attached in Tab. 4. Regarding intralaminar damage propagation, material properties must be specified in a local coordinate system that is user-defined, where the fiber direction is aligned with the local 1-direction. Due to matrix microcracking, the nonlinear behavior of the matrix—which includes both stiffness and plasticity degradation—dominates the shear response for bidirectional fiber-reinforced composites. Orthogonality between the fiber directions is assumed. With the local 1- and 2-direction aligned with the fiber directions, material properties must be specified in a user-defined local coordinate system. Damaged elasticity characterizes the material response along the fiber orientations. In addition to distinguishing between tensile and compressive fiber failure modes, the model takes into account varying initial (undamaged) stiffness in tension and compression. To define the undamaged response, therefore, bilaminar elasticity is preferred.

The material stiffness is reduced in accordance with the given damage evolution law for each specific damage initiation criterion once it is met. There is no degradation of the material stiffness without assigning a law damage evolution. The rate at which the material stiffness degrades after meeting the appropriate initiation criteria is described by the damage evolution law. The stress tensor of the material at any point during the analysis is related to the elastic strain (ε^{el}) by:

$$\sigma = C_d \varepsilon^{el} \quad (14)$$

where C_d is the matrix-damaged elasticity. Hashin damage evolution in this FE study is energy based, and the values of fracture energy are attached in Tab. 5. According to Abaqus, the deterioration of the stiffness of the matrix and fiber components can be described as a function of 3 scalar damage parameters, which correspond to the current states of shear, matrix, and fiber damage. It is necessary to use the Hashin's damage model with plane-stress elements, such as the continuum shell elements used for the composite p.v. rings throughout this study.

Shock-wave simulation parameters

The physics of wire explosion is more difficult to model than that of the application of EOS for well-studied chemical explosives because it involves a complex combination of phase transitions [28]. Previous research has proposed the governing equations for wire explosion, which include a circuit equation combined with wide-range EOS, magneto-hydrodynamic equations, and electrical conductivity for copper [29]. However, in this study, a simplified model is employed for the sake of computational efficiency and the viability of fracture analysis of composites.

It is assumed that a uniform column of vaporized products forms at the moment of explosion, and that this column expands to produce an equivalent cylindrical shock wave. One can estimate the initial conditions of this state by consulting existing literature. For example, the critical density (ϱ), boundary velocity, and plasma pressure of a 500 μm copper wire at the beginning of explosion in water with a charging voltage of 30 kV were estimated to be 2600 kg/m³, 2000 m/s, and 10 GPa, respectively [30]. In this case, at the time of explosion, the melted wire radius is roughly 0.46 mm. Furthermore, [31] reports an experimentally measured shock wave velocity of approximately 2000 m/s in the ambient air.

The specific energy deposited into the wire (E_d) determines the shock wave peak pressure and decay time. For example, $E_d = 19.44\times10^3$ kJ/kg was measured in [32] for a copper wire with a 25 μm diameter and a 20 kV discharge voltage at the air breakdown point. In [20], the deposited energy at various charging voltages is shown for wire diameters up to 240 μm. By extending these findings to a wire with a diameter of 500 μm and a 20 kV discharge, $E_d = 20\times10^3$ kJ/kg.

Under the adiabatic assumption, the ideal gas EOS is used to model the vaporized wire:

$$P = (\gamma - 1)\rho E_m \tag{15}$$

where γ denotes the isentropic index, while E_m (kJ/kg) is the internal specific energy related to E_d owing to the transformation of electric energy. The ideal gas EOS assumes the explosion products behave as a perfect gas with constant specific heats. This simplification ignores the complex phase transitions (solid-liquid-vapor-plasma) and the real gas effects of the copper vapor plasma at extremely high pressures and temperatures. The primary implication is that the initial peak pressure and the detailed temporal decay of the pressure pulse may not be perfectly captured. However, for the purpose of this study, which is to simulate the mechanical response of the composite structure to a shock pulse, the key requirements are to accurately replicate the impulse (integral of pressure over time) and the general pulse shape that loads the PMMA wall.

The published data in [19],[20],[29-32] is used to determine the EOS parameters of the exploded wire: the initial value of ϱ is equal to 2600 kg/m³ , $E_d = 20\times10^3$ kJ/kg, and the isentropic index (γ) was set to 1.4. The specific energy of copper is equal to 50 kJ/kg. In [19], further explosion experiments on pure PMMA samples were carried out to find the best fit between the numerical simulations and the experimental free-surface velocity history in order to establish the proper Equation of State (EOS), calibrating the parameters. Two discharge voltage scenarios were chosen based on earlier research on unidirectional composite cylinders: 20 kV (1.2 kJ) and 25 kV (1.875 kJ) [19]. In the EOS model, the internal energy E_m was connected to the deposited energy E_d with a correction factor that took conversion losses into account. Trial-and-error simulations were carried out using an iterative methodology, altering the pressure-internal energy relationship to correspond with experimental findings. The pressure history at a fixed Eulerian coordinate on the channel boundary confirmed consistency with previously reported experimental data. The 25% increase in discharge voltage (5 kV) resulted in a ~56% rise in stored energy, with a much greater energy conversion efficiency at higher voltages. Pressure differences between the two situations decreased over time, and the peak pressure in PMMA close to the channel was approximately 1.6 GPa for 20 kV, which was in good agreement with previous experimental observations. This process ensures that the resulting pressure pulse applied to the Lagrangian structure (PMMA/composite) in the current study FE simulations is empirically validated against physical experiments, mitigating the inaccuracies of the simplified EOS.

The discrete field of the initial Eulerian volume-fraction of the copper wire during the explosion was defined as a uniform volume-fraction-type initial condition to facilitate the CEL interaction for modeling the shock wave. To track material flow, Abaqus/Explicit employs the volume-of-fluid method, which determines the Eulerian Volume Fraction (EVF) for each element. An EVF of one indicates complete material presence, while zero signifies its absence. When the volume fraction is less than one, the remaining portion of the element is filled with "void" material, which has no mass or strength. In this

study, the void material represents air, with negligible ambient pressure of only 0.1 MPa. The initial volume fraction value of 1 was assigned to the Eulerian elements located within the central hole of the PMMA cylinder, occupying a 0.92 mm – diameter cylinder representing the copper wire region. Because the Eulerian elements are cubic, the volume fraction values ranged from 0.283 to 1 depending on whether the whole element is inside the wire region completely or partially.
CEL formulation governing the interaction between the Eulerian (vapor) and Lagrangian (PMMA and composite) domains is modeled in Abaqus/Explicit by an initial-condition-defined pressure pulse acting on the PMMA insert at the region Eulerian part inside the PMMA-composite region. Along with defining the Eulerian volume fraction, the vapor applies a pressure load P as a surface traction at the fluid-structure interface created by this conventional CEL method.
On the other hand, the Eulerian material flow is constrained by the motion of the Lagrangian boundaries, which inhibits penetration. This approach replicates the experimental transfer of energy via a shock wave through the PMMA to the composite vessel by accurately confining the expanding vapor within the channel and ensuring realistic transfer of the time-dependent pressure pulse from the expanding vapor to the structure.

Step analysis

A dynamic explicit step of 10^{-5} seconds, incorporating non-linear geometry calculations, was used to model the internal blast loading. The output requests included stress parameters, Hashin's failure criteria, and specific general contact parameters such as bond status (BDSTAT), energy release rate (ENRRT) and effective energy release rate (EFENRRTR).
Numerical viscosity is included to alleviate numerical stability issues related to explicit integration schemes. To dampen high frequencies in Abaqus, the linear bulk viscosity pressure is introduced and formulated as follows [17]:

$$p_{bvl} = b_1(\rho c_d L_e \dot{\varepsilon}_{vol}) \tag{16}$$

where b_1 is a coefficient of damping, ρ is the initial material density, c_d is the current dilatational wave speed, L_e is an element characteristic length and ε_{vol} is the risk of element collapse. Moreover, through the smearing of shock fronts across multiple elements, the quadratic bulk viscosity pressure (P_{pvc}), calculated by Eqn. (10), further reduces the risk of element collapse [17].

$$p_{bvc} = b_2(\rho L_e \dot{\varepsilon}_{vol}) \tag{17}$$

where b_2 is a damping coefficient. In high-speed impact scenarios, this is essential to avoid numerical instabilities. 0.2 and 2.4 were the optimally-selected values of b_1 and b_2 to account for the high explosion speed.

Considered Finite Element model variations of the [+45°/-45°]$_5$-orientation layup

With the same model setup explained in the preceding sections, three distinct sub-models of the [+45°/-45°]$_5$-orientation layup model were developed for further damage analysis. The first sub-model, referred to as 'Hashin's damage model', focused exclusively on analyzing in-plane failure stresses. This model only considered intralaminar damage using Hashin's failure criteria to evaluate fiber and matrix damage under in-plane stress conditions without considering spallation. The second and third ones, termed as 'total energy-release rates', or just the [+45°/-45°]$_5$-oriented layup model, and 'low energy-release rates', respectively, investigated spall damage. The second sub-model utilized VCCT energy-release rate values from [26], while the third sub-model, 'low energy-release rates', applied updated energy-release rates such that the first and second modes of energy-release rates in [27], in section 3.2, were divided by five, while the third mode value remained unchanged because the only significant mode of spallation in [19] was the first mode when compared to the other modes. This adjustment was implemented to validate the model regarding spall failure and to assess its impact on the overall vessel performance.
The overall flowchart of this study with a focus on the simulation workflow highlighting the inputs, outputs as well as elaborating the implicit constraints is shown in Fig. 6. The implicit constraints are the symmetric nature of the assembly, the radial shock wave, and the idealized connection between the PMMA insert and the composite structure all help in the effective transfer of the internal blast wave from the exploding copper vapor to the composite p.v. through the PMMA insert in the framework of CEL.

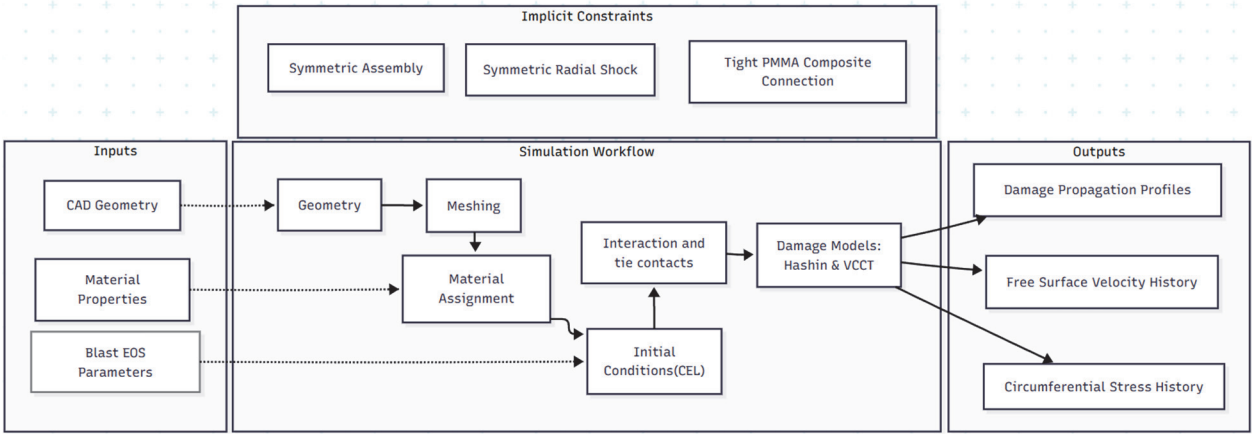

Figure 6: The summarized over all simulation workflow of the FE study.

RESULTS

Experimental results

The free surface velocity profiles of $[+45^{\circ}/-45^{\circ}]_5$ and $[0^{\circ}]_{10}$-oriented CFRP samples were recorded at varying explosive energy levels. At discharge voltages of 20 kV and 24 kV, the peak velocities for the $[+45^{\circ}/-45^{\circ}]_5$ samples were 152 m/s and 230 m/s, respectively. For the $[0^{\circ}]_{10}$-oriented samples, the peak velocities were 143.75 m/s at 20 kV and 297 m/s at 25 kV. The observed failure modes indicate that circumferential shear stress (τ_{12}) dominated in the $[+45^{\circ}/-45^{\circ}]_5$ samples. For the $[0^{\circ}]_{10}$-oriented CFRP samples, the circumferential strain (ε_{ϑ}) of the outer composite shell and the strain rate (e_{ϑ}) can be determined by numerically integrating the free surface velocity (v_{fs}) to obtain the displacement in the radial direction (u_r):

$$\varepsilon_{\vartheta} = \frac{u_r}{R}; e_{\vartheta} = \frac{v_{fs}}{R} \tag{18}$$

where R is the inner radius of the specimen composite shell. The longitudinal tensile failure stresses of the $[0^{\circ}]_{10}$-oriented structures were 2142 MPa and 3528 MPa for the 20 kV and 25 kV tests, respectively. They are calculated based on Young's modulus.

As for the $[+45^{\circ}/-45^{\circ}]_5$-oriented samples, the experimental results of [19] indicate that increased deposited specific energy into the electric wire (higher voltage and higher pressure) led to localized failure near the free edge of the $[+45^{\circ}/-45^{\circ}]_5$ samples. Based on layup orientation, the stiffness matrix is computed to estimate failure shear stress. The ordinary stiffness matrix (Q) at $[0^{\circ}]_{10}$ orientation is formulated as follows:

$$\begin{pmatrix} Q_{11} & Q_{12} & Q_{16} \\ Q_{12} & Q_{22} & Q_{26} \\ Q_{16} & Q_{26} & Q_{66} \end{pmatrix} = \begin{pmatrix} \frac{E_1}{Y} & \frac{\upsilon_{12}E_2}{Y} & 0 \\ \frac{\upsilon_{12}E_2}{Y} & \frac{E_2}{Y} & 0 \\ 0 & 0 & G_{12} \end{pmatrix} \tag{19}$$

where E_1 = 126 GPa, E_2 = 8.2 GPa, υ_{12} = 0.33, $Y = 1 - (E_2/E_1)\,\upsilon_{12}^2$, and G_{12} = 3.2 GPa. Therefore, the elements of the $[+45°/-45°]_5$ stiffness matrix ($Q^{\pm 45}$) are determined from the ordinary stiffness matrix elements as:

$$Q_{11}^{\pm 45} = Q_{22}^{\pm 45} = \frac{1}{4}Q_{11} + \frac{1}{4}Q_{22} + \frac{1}{2}(Q_{12} + 2Q_{66})$$

$$Q_{12}^{\pm 45} = \frac{1}{4}(Q_{11} + Q_{22} - 4Q_{66}) + \frac{1}{2}Q_{12} \tag{20}$$

$$Q_{66}^{\pm 45} = \frac{1}{4}(Q_{11} + Q_{22} - 2Q_{12})$$

$$Q_{16}^{\pm 45} = Q_{26}^{\pm 45} = 0$$

ε_y can be estimated thanks to the definition of a compliance matrix, which is defined as $S^{\pm 45} = [Q^{\pm 45}]^{-1}$. The strain in the direction of the cylinder axis is estimated using the effective engineering constants, $E_1^{\pm 45}$ equal to $(S_{11}^{\pm 45})^{-1}$ and $\nu_{12}^{\pm 45}$ which is determined by:

$$\nu_{12}^{\pm 45} = S_{12}^{\pm 45} E_1^{\pm 45} = \frac{S_{12}^{\pm 45}}{S_{11}^{\pm 45}} \tag{21}$$

Shear stress (τ_{12}) is calculated based on the shear strain in the ply coordinates (γ_{12}) as:

$$\gamma_{12} = -\varepsilon_{xx} sin(2\theta) + \varepsilon_{yy} sin(2\theta) + \gamma_{xy} \cos(2\theta)$$

$$\tau_{12} = G_{12}\gamma_{12} \tag{22}$$

where x is the geometry x-axis direction which coincides with the circumferential direction, y is the cylindrical axis direction, and the circumferential strain ε_{xx} is equal to ε_y. γ_{12} is calculated based on the transformation law from global to ply coordinates, and θ is the angle of rotation equal to $[+45^\circ/-45^\circ]_5$ in the current layup.
The calculated circumferential shear failure stresses (τ_{12}) were 47 MPa and 129 MPa, which aligns closely with the static failure stress of 48 MPa, and 129 MPa for the 20 kV and 24 kV tests, respectively.

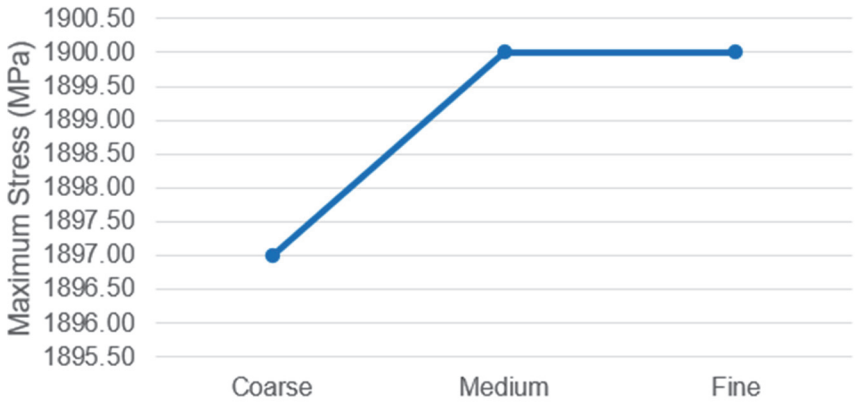

Figure 7: Mesh study analysis of the FEA simulations.

Mesh convergence study

A mesh sensitivity analysis was performed based on tensile failure stress. As depicted in Fig. 7, the coarse mesh yielded a tensile failure stress of 1897 MPa, while both the medium and fine meshes converged at 1900 MPa. This indicates that the FEA simulation models are following a convergent pattern and there is no mesh dependency. It is noted that the number

of points for the study is limited because the coarse mesh was already created finely to ensure having acceptable results, thus more refinement was challenging and computationally difficult considering the available resources for this study.

Numerical simulation results

The Hashin's fiber-tensile failure initiation criterion of the $[+45^{\circ}/-45^{\circ}]_5$-oriented layup (HSNFTCRT) was first reached at 5.24 μs under a tensile stress of 1898 MPa, while the fiber-compressive failure criterion (HSNFCCRT) was triggered at 5.68 μs at a compressive stress of 613 MPa. Matrix compressive failure (HSNMCCRT) was observed at 3.7 μs when the compressive stress reached 124 MPa, and matrix tensile failure (HSNMTCRT) occurred at 3.26 μs under a transverse tensile stress of 18 MPa. These values indicate when the intralaminar damage was initiated and what the values of failure stress were equal to. It is noted that the damage in fibers due to tension was the last to initiate because the material tensile strength in the direction of fibers is the highest strength value (1898 MPa). It is noted that planar damage initiation starts first at matrix then it propagates till fiber damage indicating the progressive damage nature. For example, matrix compression failed first (3.7 μs), followed by fiber tension (5.24 μs), indicating damage propagation.

The free surface velocity and corresponding nodal fiber tensile stress curves of the $[+45^{\circ}/-45^{\circ}]_5$ and the $[0^{\circ}]_{10}$ oriented layups at a critical node on the outer surface at the vessel mid-length are illustrated in Fig. 8, respectively. The maximum velocity component in the x-direction for the $[+45^{\circ}/-45^{\circ}]_5$ layup was 168 m/s, while for the $[0^{\circ}]_{10}$ layup, it was 157 m/s. Due to the vessel symmetry, the x-direction velocity value at the selected node is a representative of the radial shock wave propagation speed at any point on the circumference passing through the selected node. Since the reflected tensile wave from this free surface is the main cause of spallation damage, the node chosen for Fig. 6 is situated on the outer surface at the mid-length of the vessel and represents a critical response region for two main reasons: it corresponds to the experimental measurement point for free-surface velocity obtained via laser interferometry [19], allowing direct validation of the simulation, and it is a region of high importance for failure assessment. Direct knowledge of the p.v. dynamic response can be gained from the stress history captured at this node. The shock wave arrival at the node is indicated by the radial wave speed change. As it passes through the PMMA and composite layers, the explosion outward-propagating compressive shock wave arrive after 3 μs. This is followed by the onset of matrix failure: matrix tensile and matrix compressive at 3.26 μs and 3.7 μs for the $[+45^{\circ}/-45^{\circ}]_5$ layup, and at 3.2 μs and 4.6 μs for the $[0^{\circ}]_{10}$ layup, respectively. The radial velocity first peak is reached at 4 μs at a nodal fiber tensile stress equal to 500 MPa. Then, while the fiber tensile stress is increasing, the radial speed starts decay till reaching 25 m/s at 4.5 μs indicating wave reflection from the outer surface till reaching a second peak velocity equal to 137 m/s at 5 μs, the process which explains the activation of VCCT interlaminar debonding of the $[+45^{\circ}/-45^{\circ}]_5$ layup at 4.52 μs. This confirms the reflected tensile wave is the driving mechanism for spallation. The second velocity peak is followed by the fiber tensile stress peak equal to 1310-1375 MPa at 5.1-8.8 μs. This is accompanied by the onset of fiber failure: fiber tensile and fiber compressive at 5.2 μs and 5.7 μs for the $[+45^{\circ}/-45^{\circ}]_5$ layup.

It is noted that fiber tensile stress depicted in Fig. 6 indicates a simultaneous radial (out-of-plane) matrix-compressive stress due to the radial propagation of the shock wave, while the reflected wave from the free surface creates a radial matrix matrix-tensile stress and a simultaneous fiber compressive stress. The subsequent fiber-compressive/radial matrix-tensile stress region (6.75–10 μs) corresponds to the reflection of the shock wave from the free surface penetrating again into the specimen. In the later period of the stress history, wave reverberations in the layered structure are established and the decay in wave amplitudes is associated with damage accumulation and energy dissipation through fracture surface generation and permanent reduction in load carrying capacity. Accordingly, the initiation of each stress peak is associated with the blast loading process, which in turn connects wave interactions to the responsible failure mechanisms in the vessel: intralaminar and interlaminar damages.

The evolution of spall damage of the $[+45^{\circ}/-45^{\circ}]_5$ layup is illustrated in Fig. 9(a). The first mode of fracture played a dominant role in spall failure, although the second mode reached its critical value at one node within the assembly. The spatial distribution of the energy-release rates explains the physical mechanism of spallation failure. The middle layers plies of the composite vessel, specifically the interfaces closer to the PMMA insert, are where spallation is always started. This location is a direct consequence of the stress wave dynamics within the structure: shock wave propagation and reflection, and complex interaction between compressive and reflected tensile radial waves. The first compressive shock wave produced by the wire explosion is transmitted to the composite shell through the PMMA insert then reflects as a tensile wave when it reaches the vessel free surface. When the tensile reflected wave moves inward, a region of high tensile triaxiality is produced due to its interaction with the still-incoming compressive wavefront. High Mode-I (opening) strains are caused by the impedance mismatch between composite plies of different orientations and at the PMMA-composite interface, which makes this interfacial region a major site for stress wave amplification. Compared to the $[+45^{\circ}/-45^{\circ}]_5$ layup, this explains why spallation damage is not dominant in the $[0^{\circ}]_{10}$ layup because spallation is mainly noticed at the PMMA-composite interface because all the plies have the same orientation.

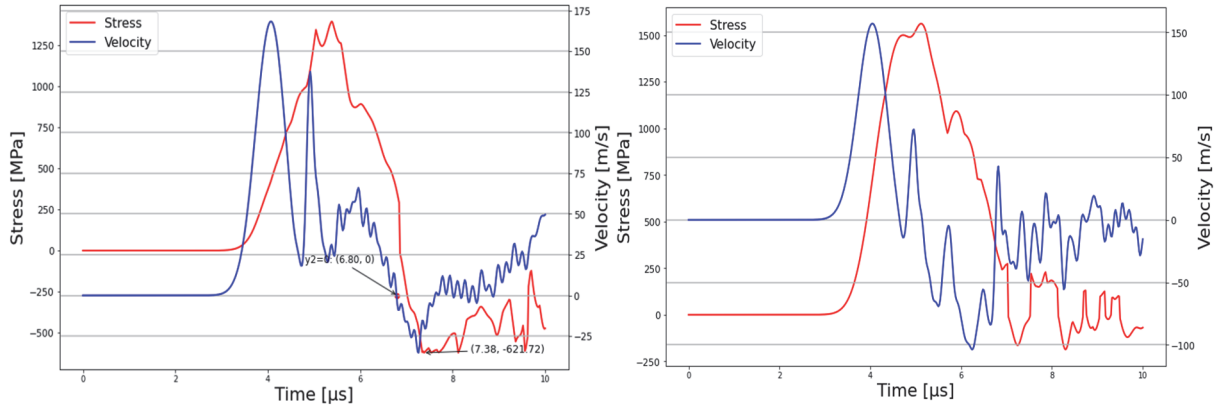

(a) (b)

Figure 8: Spall x-axis velocity and corresponding stress change at a critical node on the outer surface at the vessel mid-length for the $[+45^{\circ}/-45^{\circ}]_5$ lay-up (a) and the $[0^{\circ}]_{10}$ lay-up (b).

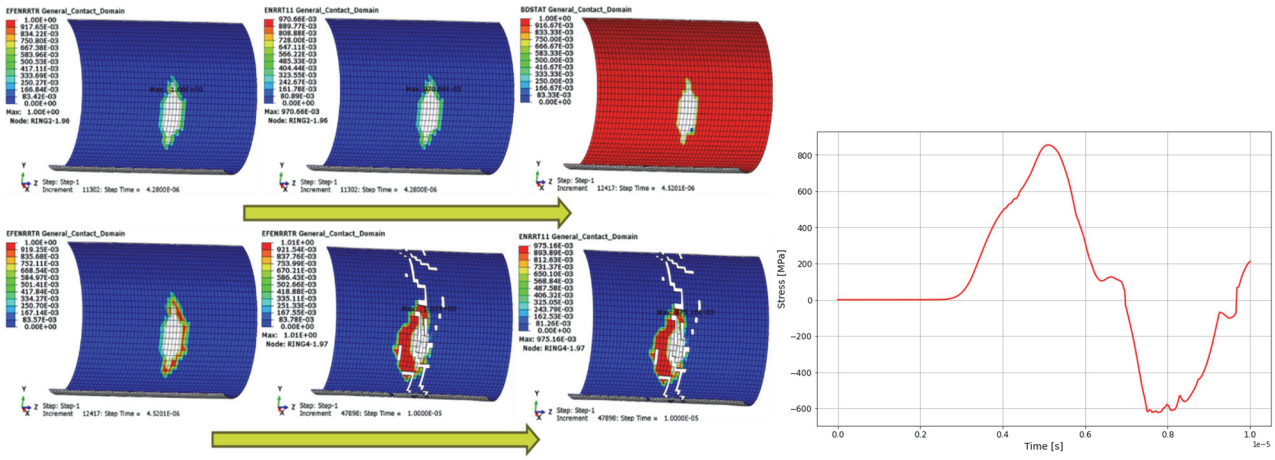

(a) (b)

Figure 9: Spall Evolution of the $[+45°/-45°]_5$ orientation lay-up (a) and the representative curve of the stress change due to explosion (b).

The experimental post-mortem observations documented in [19], which revealed extensive internal delamination and fiber breakage at the $[+45^{\circ}/-45^{\circ}]_5$ layup support this predicted failure origin. The numerical results predominance of the first mode of energy release rate (g_I) verifies that through-thickness tensile stress ("hoop-opening") brought on by wave reflection, rather than in-plane shear, is the main cause of spallation. As a result, the dynamic interaction between the imposed shock wave and the vessel geometry is what causes the spallation. The most vulnerable area and the main failure mode are identified by the model, which effectively captures the basic physics of this event. This information is essential for designing vessels with enhanced blast resistance.

Fig. 9(b) provides a representative stress curve at a selected node in the model that is located at the outer surface of the inner ring at the vessel mid-length, highlighting nearly symmetric tension and compression states due to shock wave propagation and reflection. The selected node corresponds to the location where the maximum fiber compressive stress (accompanying the radial matrix-tensile stress) was observed on the inner ring.

The final maximum values of the energy-release rate 3 modes are illustrated in Fig. 10. The snippets indicate that only the first mode is more responsible for the spall failure in our model, despite that the 2nd mode reached the critical value as it was achieved only at one node.

However, for the 'low energy-release rates' model, HSNFTCRT was triggered at 5.62 μs with a failure stress of 1894 MPa, while HSNFCCRT occurred at 5.42 μs at 619 MPa. Additionally, HSNMCCRT was reached at 3.62 μs at a compressive stress of 120 MPa, and HSNMTCRT at 3.26 μs under a transverse tensile stress of 18.26 MPa.

The effective energy release rate (EFENRRTR) was first reached at 4.14 μs when $g_I = 0.289$, exceeding its critical value ($g_{IC} = 0.194$). The second and third modes at the same time instance remained below their critical thresholds, with $g_{II} = 0.169$

(g_{IIc} = 0.250) and g_{III} = 0.418 (g_{IIIc} = 1.25). In ring 9, the second mode energy-release rate (ENRRT12), g_{II}, reached 0.249, closely matching its input critical value of 0.250. This confirms the hypothesis that spall damage was more evident in this model rather than the model with the original energy release rates from [27]. This finding clarifies that this numerical model is faithfully representing the interlaminar and intralaminar damages noticed in the experimental testing of the [+45°/-45°]$_5$-oriented samples.

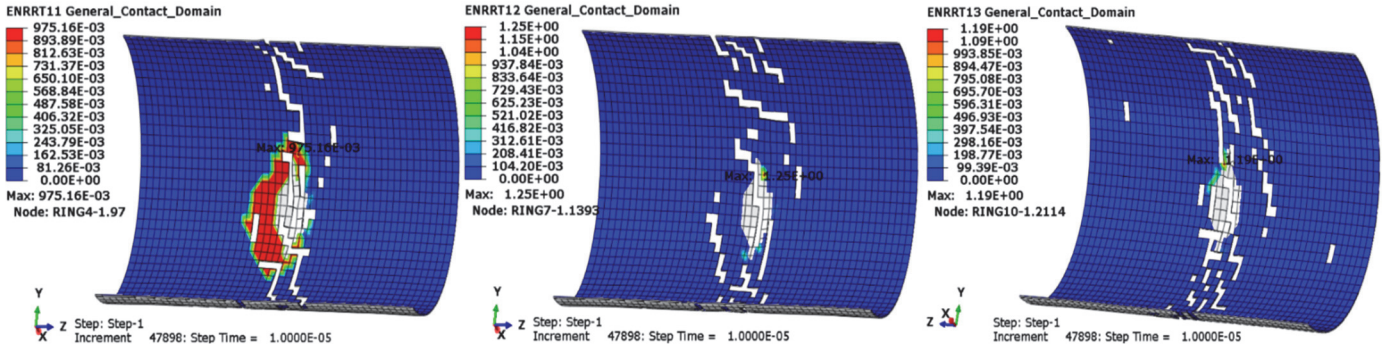

(a) (b) (c)

Figure 10: a) Energy-release rate first mode b) Energy-release rate second mode c) Energy-release rate third mode.

In addition, comparative study was conducted using a model with only Hashin's planar damage criterion to assess deviations from experimental observations. The negligible HSNFTCRT values in this model further substantiate the presence of spall damage in the experiments. Tab. 6 summarizes Hashin's failure initiation criteria across different models, where F.T is fiber tensile; F.C is fiber compressive; M.C is matrix compressive; and M.T is matrix tensile Hashin's initiation criteria. The mechanism of vessel failure under internal blast loading can be clearly explained by the thorough chronology of Hashin damage initiation criteria. For example, the observed sequence of Hashin damage initiation of the [+45°/-45°]$_5$ layup: matrix tensile failure (3.26 μs), matrix compressive failure (3.7 μs), fiber tensile failure (5.24 μs), and fiber compressive failure (5.68 μs) indicates a progressive decay of the composite ability to carry load. The compressive shock wave and its reflections cause through-thickness shear and transverse normal stresses, which in turn cause initial matrix failures. Even Before VCCT delamination starts, this matrix damage accelerates the debonding process by instantly reducing interlaminar shear transfer and degrading stiffness perpendicular to the fibers.

Peak hoop stresses (planar tensile stresses) brought on by internal pressure correspond with subsequent fiber failures. The hoop-driven loading in pressurized vessels is consistent with fiber tensile failure predominating over compressive failure. At this point, the ultimate load is carried until rupture by fibers that are already unsupported by the deteriorated matrix. This sequence illustrates a typical composite failure progression where catastrophic fiber failure is caused by the matrix acting as the first weak link. The occurrence of all events within the first 6 μs highlights how quickly blast loading occurs and validates that the model accurately depicts the intricate, rate-dependent competition between failure modes.

Model	F.T (s)/(MPa)	F.C (s)/(MPa)	M.C (s)/(MPa)	M.T (s)/(MPa)
[+45°/-45°]$_5$, only planar damage	No failure initiated	7.9 / 621	4.8 / 120	3.2 / 18.2
[+45°/-45°]$_5$, low energy-release rates	5.6 / 1894	5.4 / 619	3.6 / 87	3.3 / 18.3
[+45°/-45°]$_5$	5.2 / 1898	5.7 / 622	3.7 / 87	3.3 / 18.3
[0°]$_{10}$	4.9 / 1920	8.3 / 620	4.6 / 124	3.2 / 18.3

Table 6: Comparing the used models based on the in-plane Hashin's damage.

Model validation

To validate the simulation models and approve the results of intra-laminar and inter-laminar damages, the numerical results of free surface velocities and failure stresses are compared with the experimental results. Fig. 11 shows that the numerical velocity of the [+45°/-45°]$_5$ -oriented sample on the outer surface is close to the recorded experimental velocity by following a similar profile having the peak values so close. At 20 kV discharge, as in Fig. 10, the velocity peak values of the numerical models with the [+45°/-45°]$_5$ and [0°]$_{10}$ orientations, are 165.2 m/s and 159 m/s, a little bit greater than the experimental

ones, 152 m/s and 143.75 m/s, correspondingly. This means the accuracy of the $[+45^{\circ}/-45^{\circ}]_5$ oriented model compared to the experiment is roughly equal to 92.0 %, while it is 90.6 % for the $[0^{\circ}]_{10}$ orientated sample. This small difference can be explained that the numerical velocity curves are recorded on the nodes that experienced the highest velocities, while the experimental velocity was recorded only at the pre-defined location of the laser interferometer (no guarantee its location is where the maximum speed is). Moreover, the slight over-predicted FE velocity in both layups is logically attributed to the perfectly-symmetric ideal initial conditions applied through the CEL framework where the shock wave is defined, as well as the symmetric nature of the developed model setup. In addition, the idealized tie contact between the outer surface of the PMMA insert and the inner surface of the first CFRP composite ply increases the efficiency of transferring the shock wave from the PMMA insert to the composite p.v. shell.

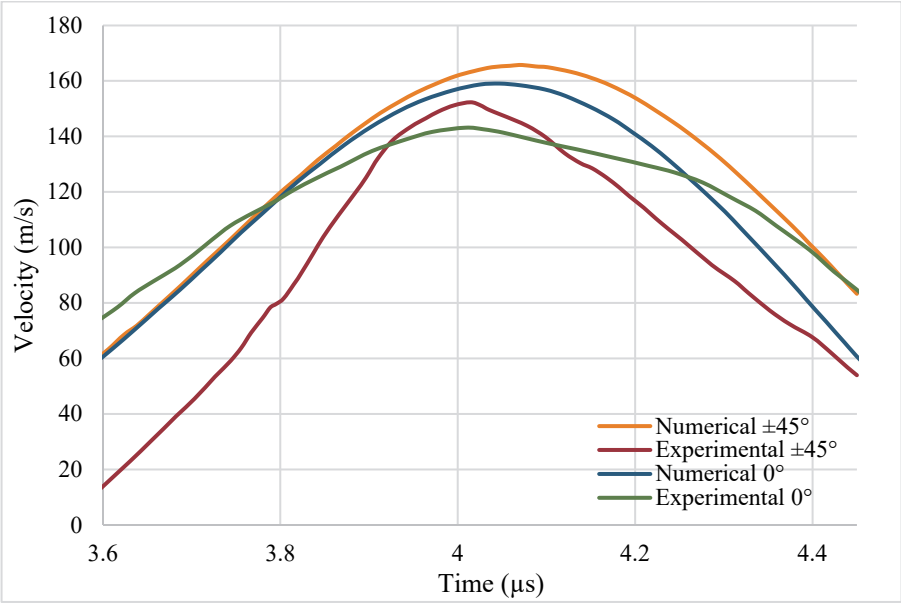

Figure 11: Experimental and numerical velocities comparison of the $[+45^{\circ}/-45^{\circ}]_5$-oriented vessels.

Additionally, for further validation, the experimental shear failure stress was compared to the experimental one for the $[+45^{\circ}/-45^{\circ}]_5$ fiber-oriented samples. The numerical values are based on the finest mesh of the FE model to ensure reliable results. The numerical failure shear stress is equal to 47.9 MPa while the experimental one was equal to 47.0 MPa, meaning the accuracy is 98.1 %. The reason why the experimental dynamic value is so close to the experimental static value is that in CFRP static shear tests, the loading diagram usually shows nonlinearity because the sample locally accumulates damage well below the maximum force [19]. Moreover, the numerical tensile failure stress of the $[0^{\circ}]_{10}$fiber-oriented model is equal to 1900 MPa while the experimental one was equal to 2142 MPa, which is only around 11.3% difference compared to the reference model in [19] where no damage was introduced. This difference is because the experimental velocities are calculated by integrating the interferometer recorded velocities, that are not guaranteed to be capturing the highest velocity, thus yielding into lower displacements [19]. More importantly, it is also noticed that this numerical failure stress value is greater than the failure stress value of 1890 MPa in [19], meaning that a better accuracy in terms of failure stress was achieved after introducing the inter-laminar and intra-laminar damage models. These stress analysis findings, along with attaining similar numerical damage and outer-layer velocity profiles to the experiments, indicate that the simulation models can be used to predict the composite pressure vessels (p.v.) under internal blast loading conditions.

Discussion

This study combines numerical simulations and experimental analysis to understand how composite materials, particularly CFRP confinement vessels, behave under explosive loading scenarios. Although there is moderate agreement between the resulting velocity profiles in the experiments and the FE models, discrepancies suggest that more work is needed to improve predictive models. Issues such as wave reverberations, limitations in material models, and flaws in wire alignment within explosive channels need to be addressed to produce more efficient models of internal explosion tests.

The use of quasi-static material properties in the current high-strain-rate model was a considered decision based on the specific context of this study and the available literature. For the unidirectional (0°) samples, the dynamic tensile strength calculated from free-surface velocity (2142 MPa at 20 kV) was only ~12 % higher than the quasi-static strength (1898 MPa) [19]. And for the ±45° samples, the dynamic shear failure stress at 20 kV (47 MPa) was found to be nearly identical to the upper-bound static value (48 MPa). This relatively weak strain-rate sensitivity, especially at the lower energy discharge (20 kV) which our FE model closely replicates, suggests that a quasi-static baseline is a reasonable first approximation for the intralaminar material model. The most significant limitation is that our model cannot predict the strength increase observed at higher strain rates. The model will initiate intralaminar damage at the quasi-static strength values, potentially leading to an over-prediction of damage and an under-prediction of the stress wave magnitude propagating through the structure at higher energy levels. This is a likely contributor to the observed discrepancies in peak velocity and stress at higher voltages.
To improve the accuracy of the predictive model, the study calibrates EOS vapor parameters and combines experimental analysis with numerical simulations. Adjusted EOS vapor parameters ensure better agreement between experimental findings and numerical simulations, enhancing the accuracy of predictive models for well-informed choices in contrast to previous studies with limited EOS numerical validations on the PMMA material [28]. The calibrated ideal gas approach in this study was deemed the best compromise between physical accuracy and computational feasibility for this specific engineering application and more complex EOS would be computationally inefficient.
Observed failure modes in the angle-ply composite samples highlight the importance of considering edge effects and fiber orientations in structural design. The shear stress' effect was significant in the angle-ply (±45°) composite sample, resulting in a complex failure mode compared to the unidirectional 0° composite sample. Failure analysis on the composite vessels, as a further step to the work in [19], was performed to understand the composite shell in-plane failure and inter-laminar damage using in-plane failure criteria and inter-laminar damage models of crack initiation and propagation. This approach resulted in a more comprehensive understanding of failure onset and progression, improving structural response predictions in harsh circumstances. Future research should focus on improving predictive models, broadening experimental investigations, and investigating novel materials and structural arrangements to improve safety and performance in high-risk situations, especially at higher explosion energies.

CONCLUSIONS

In this study, the response of CFRP confinement vessels to internal explosive loading was comprehensively analyzed through numerical simulations validated against experimental data. The research aims were to elucidate failure mechanisms and damage propagation patterns in these materials. Simulations and experiments on unidirectional and angle-ply composites demonstrated good agreement, with 90.6% and 92% accuracy in velocity prediction and 88.7% and 98.1% in failure stress validation, correspondingly. Remaining discrepancies of 8–11.3% were attributed primarily to wave dispersion effects and boundary condition idealizations, reflecting both the capabilities and challenges of the current modeling framework in fully capturing the complex dynamic response. Observed failure modes, including fiber rupture and shear failure, provided critical insights into the behavior of composite structures under extreme loading, though the rate-independent nature of the Hashin and VCCT criteria limits accuracy at very high strain rates.
The findings of this study are pivotal for advancing the design and risk-mitigation strategies of composite pressure vessels in high-risk environments, enabling the development of more effective safety measures. current modeling limitations by incorporating strain-rate-dependent material formulations, refining boundary condition representations to minimize wave propagation errors, and expanding validation to various explosion energies. The refinement of analytical models and numerical simulations could help better capture the intricate behavior of composite materials under explosive loading. Expanding future experimental and numerical studies to include a broader range of composite materials and loading conditions will further enhance the accuracy and applicability of the VCCT and Hashin numerical models.
Despite identified limitations, this work represents an advancement in understanding the response of CFRP composite p.v. to explosive events. The developed CEL-based finite element framework simultaneously captures in-plane stress and spall damages under internal blast loading, offering a validated computational approach for designing blast-resistant CFRP structures. Its good alignment with experimental results underscores both its practical value and its improvement over previous methodologies, providing detailed insights into high-strain-rate effects and supporting the reliable design and production of composite pressure vessels for high-risk applications.

ACKNOWLEDGEMENT

This study was carried out under the Agreement for the provision of grant funding from the federal budget for large scientific projects in priority areas of scientific and technological development of the Russian Ministry of Science and Higher Education no. 075-15-2024-552.

CREDIT AUTHORSHIP CONTRIBUTION STATEMENT

Kamal M. Hammad: Writing – original draft, Writing – review and editing, Investigation, Conceptualization, Methodology, Visualization, Software, Investigation. Iuliia A. Sadykova: Conceptualization. Eugene N. Prokopev: Visualization. Galina V. Tyurina: Conceptualization. Semen D. Ignatyev: Visualization. Eugene S. Statnik: Writing – review and editing.

DECLARATION OF COMPETING INTEREST

The authors declare that they have no known competing financial interests or personal relationships that could have appeared to influence the work reported in this paper.

REFERENCES

[1] Czichos, R., Middendorf, P., Bergmann, T. (2022). Numerical modelling of the residual burst pressure of thick composite pressure vessels after low-velocity impact loading., Current Perspectives and New Directions in Mechanics, Modelling and Design of Structural Systems, 1st ed., London, CRC Press, pp. 157–158.

[2] Yuan, Q., Chen, H., Gu, W., Wang, Z., Hao, L. (2021). Anti-explosion Capability and Impact Response of an Innovative Multi-layered Composite Explosion Containment Vessel. DOI: https://doi.org/10.21203/rs.3.rs-837089/v1.

[3] Hong, H. (2016). Burst Strength Analysis of Composite Pressure Vessel using Finite Element Method.

[4] Korsunsky, A.M., (2024). The Rational Experimental-Computational Correlation (RECC) – reliability improvement toolkit for materials technologies in aerospace design., ISSI 2024, conference, Dongguan, China.

[5] Rajak, D.K., Pagar, D.D., Menezes, P.L., Linul, E. (2019). Fiber-Reinforced Polymer Composites: Manufacturing, Properties, and Applications, Polymers, 11(10), p. 1667. DOI: https://doi.org/10.3390/polym11101667.

[6] Jayan, J.S., Appukuttan, S., Wilson, R., Joseph, K., George, G., Oksman, K. (2021). 1 - An introduction to fiber reinforced composite materials., In: Joseph, K., Oksman, K., George, G., Wilson, R., Appukuttan, S. eds., Fiber Reinforced Composites, Woodhead Publishing, pp. 1–24.

[7] Hosseini, E., Popovich, V.A. (2019). A review of mechanical properties of additively manufactured Inconel 718, Additive Manufacturing, 30, p. 100877. DOI: https://doi.org/10.1016/j.addma.2019.100877.

[8] Al-Mosawe, A., Al-Mahaidi, R., Zhao, X.-L. (2017). Engineering properties of CFRP laminate under high strain rates, Composite Structures, 180, pp. 9–15. DOI: https://doi.org/10.1016/j.compstruct.2017.08.005.

[9] Yao, Y., Cui, J., Wang, S., Xu, L., Li, G., Pan, H., Bai, X. (2022). Comparison of Tensile Properties of Carbon Fiber, Basalt Fiber and Hybrid Fiber Reinforced Composites Under Various Strain Rates, Appl Compos Mater, 29(3), pp. 1147–1165. DOI: https://doi.org/10.1007/s10443-022-10012-9.

[10] Lomakin, E., Fedulov, B., Fedorenko, A. (2021). Strain rate influence on hardening and damage characteristics of composite materials, Acta Mech, 232(5), pp. 1875–1887. DOI: https://doi.org/10.1007/s00707-020-02806-4.

[11] Ahmed, A., Zillur Rahman, M., Ou, Y., Liu, S., Mobasher, B., Guo, S., Zhu, D. (2021). A review on the tensile behavior of fiber-reinforced polymer composites under varying strain rates and temperatures, Construction and Building Materials, 294, p. 123565. DOI: https://doi.org/10.1016/j.conbuildmat.2021.123565.

[12] Costas, M., Díaz, J., Romera, L.E., Hernández, S., Tielas, A. (2013). Static and dynamic axial crushing analysis of car frontal impact hybrid absorbers, International Journal of Impact Engineering, 62, pp. 166–181. DOI: https://doi.org/10.1016/j.ijimpeng.2013.06.011.

[13] Murthy, V.C.A.D., Santhanakrishnanan, S. (2020). Isogrid lattice structure for armouring applications, Procedia Manufacturing, 48, pp. e1–e11. DOI: https://doi.org/10.1016/j.promfg.2020.05.099.

[14] Skaar, M.W. (2015). Modeling and Testing of Impact Damage in Composite Pressure Vessels. Master thesis, NTNU.
[15] Belabed, Z. (2025). A new application of quadrilateral finite element model incorporating the discrete shear projection technique for free vibration response of CNT reinforced plates, International Journal of Solids and Structures, 309, p. 113204. DOI: https://doi.org/10.1016/j.ijsolstr.2024.113204.
[16] Belabed, Z., Taibi, N., Boucham, B., Benguediab, M., Tounsi, A., Khedher, K.M., Salem, M.A. (2023). On the Thermomechanical Behavior of Laminated Composite Plates using different Micromechanical-Based Models for Coefficients of Thermal Expansion CTE), J. Appl. Comput. Mech., (Online First). DOI: https://doi.org/10.22055/jacm.2023.44257.4191.
[17] Guerine, M.H.E., Belabed, Z., Tounsi, A., Mohamed, S.M.Y., Althobaiti, S., Selim, M.M. (2024). On the free vibration behavior of carbon nanotube reinforced nanocomposite shells: A novel integral higher order shear theory approach, Structural Engineering and Mechanics, 91(1), pp. 1–23. DOI: https://doi.org/10.12989/SEM.2024.91.1.001.
[18] Hadj Meliani, M., Kenanda, M.A., Hammadi, F., Belabed, Z. (2023). Free vibration analysis of the structural integrity on the porous functionally graded plates using a novel Quasi-3D hyperbolic high order shear deformation theory, Frattura Ed Integrità Strutturale, 17(64), pp. 266–282. DOI: https://doi.org/10.3221/IGF-ESIS.64.18.
[19] Fedorenko, A., Sudenkov, Y., Konev, S., Sergeichev, I. (2023). Exploding wire method for the characterization of dynamic tensile strength of composite materials, International Journal of Impact Engineering, 180, p. 104704. DOI: https://doi.org/10.1016/j.ijimpeng.2023.104704.
[20] Batra, A. C., Jaiswar, R., Valvi, and Kaushik, T. C. (2019). Experimental Investigations on Specific Energy Deposition and Burst Characteristics in Electrically Exploded Single Copper Wires, IEEE Trans. Plasma Sci., 47(1), pp. 596–602. DOI: https://doi.org/10.1109/TPS.2018.2870480.
[21] Wan, L., Ullah, Z., Yang, D. and Falzon, B. G. (2023). Comprehensive inter-fibre failure analysis and failure criteria comparison for composite materials using micromechanical modelling under biaxial loading, J. Compos. Mater., 57(18), pp. 2919–2932. DOI: https://doi.org/10.1177/00219983231176609.
[22] ABAQUS Analysis User's Manual (v6.6). (n.d.). Available at: https://classes.engineering.wustl.edu/2009/spring/mase5513/abaqus/docs/v6.6/books/usb/default.htm?startat=pt06ch23s06alm15.html.
[23] Seo, H., Hundley, J., Hahn, H.T., Yang, J.-M. (2010). Numerical Simulation of Glass-Fiber-Reinforced Aluminum Laminates with Diverse Impact Damage, AIAA Journal, 48(3), pp. 676–687. DOI: https://doi.org/10.2514/1.45551.
[24] Murphy, J.G. (2013). Transversely isotropic biological, soft tissue must be modelled using both anisotropic invariants, European Journal of Mechanics - A/Solids, 42, pp. 90–96. DOI: https://doi.org/10.1016/j.euromechsol.2013.04.003.
[25] Rappolt, J.T. (2015). Analysis of a Carbon Fiber Reinforced Polymer Impact Attenuator for a Formula SAE Vehicle Using Finite Element Analysis. California Polytechnic State University, San Luis Obispo, California.
[26] Benzeggagh, M.L., Kenane, M. (1996). Measurement of mixed-mode delamination fracture toughness of unidirectional glass/epoxy composites with mixed-mode bending apparatus, Composites Science and Technology, 56(4), pp. 439–449. DOI: https://doi.org/10.1016/0266-3538(96)00005-X.
[27] Ibrahim, G.R. (2023). Progressive Damage Modelling of Composite Materials. doctoral, Manchester Metropolitan University.
[28] Romanova, V.M., Ivanenkov, G.V., Mingaleev, A.R., Ter-Oganesyan, A.E., Shelkovenko, T.A., Pikuz, S.A. (2015). Electric explosion of fine wires: Three groups of materials, Plasma Phys. Rep., 41(8), pp. 617–636. DOI: https://doi.org/10.1134/S1063780X15080085.
[29] Chung, K.-J., Lee, K., Hwang, Y. S. and Kim, D.-K. (2016). Numerical model for electrical explosion of copper wires in water," J. Appl. Phys., 120(20), p. 203301. DOI: https://doi.org/10.1063/1.4968396.
[30] Li, X., Chao, Y., Wu, J., Han, R., Zhou, H. and Qiu, A. (2015). Study of the shock waves characteristics generated by underwater electrical wire explosion, J. Appl. Phys., 118(2), 023301, DOI: https://doi.org/10.1063/1.4926374.
[31] Barbaglia M. and Rodríguez Prieto, G. (2016). Temporal shock wave analysis produced by copper exploding wires in air at atmospheric pressure, Phys. Plasmas, 23(10), p. 102706. DOI: https://doi.org/10.1063/1.4966140.
[32] Pikuz, S. A., Tkachenko, S. I., Romanova, V. M., Shelkovenko, T. A., Ter-Oganesyan, A. E. and Mingaleev, A. R. (2006). Maximum Energy Deposition During Resistive Stage and Overvoltage at Current Driven Nanosecond Wire Explosion, IEEE Trans. Plasma Sci., 34(5), pp. 2330–2335, DOI: https://doi.org/10.1109/TPS.2006.878364.